scientific reports

OPEN

Synthesis of ternary copper antimony sulfide via solventless thermolysis or aerosol assisted chemical vapour deposition using metal dithiocarbamates

Fadiyah Makin[1,2], Firoz Alam[3], Mark A. Buckingham[1] & David J. Lewis[1✉]

Copper antimony sulfide (Cu-Sb-S) has recently been proposed as an attractive alternative photovoltaic material due to the earth-abundant and non-toxic nature of the elements, high absorption coefficients and band gaps commensurate with efficient harvesting of solar photonic flux across multiple phases of Cu-Sb-S. These materials are therefore highly desirable and sustainable and scalable deposition techniques to produce them are of interest. In this paper, we demonstrate two facile, low-temperature and inexpensive techniques (solventless thermolysis and aerosol-assisted chemical vapor deposition (AACVD)) for the preparation of binary digenite ($Cu_{1.8}S$), chalcocite (Cu_2S) and stibnite (Sb_2S_3) and several phases of ternary copper-antimony-sulfide ($Cu_{2x}Sb_{2(1-x)}S_y$, where $0 \le x \le 1$). It was found that by utilising these different techniques and varying the ratio of Cu:Sb, pure phases of ternary chalcostibite ($CuSbS_2$), fematinite (Cu_3SbS_4) and tetrahedrite ($Cu_{12}Sb_4S_{13}$) can be achieved. Two single-source precursors were investigated for this purpose, namely the diethyldithiocarbamate (DTC) complexes of copper and antimony $Cu(DTC)_2$ and $Sb(DTC)_3$. These were decomposed both individually (to produce binary materials) and combined (to produce ternary materials) at different ratios. From the solventless thermolysis and AACVD methods, either particulate or thin film material was formed, respectively. These materials were then characterised by powder XRD, SEM, EDX and Raman spectroscopies to determine the crystalline phase, material morphology and uniformity of elemental composition. This analysis demonstrated that as the Cu-content increases, the phase of the ternary material changes from chalcostibite ($CuSbS_2$) and fematinite (Cu_3SbS_4) at a low Cu:Sb ratio to tetrahedrite ($Cu_{12}Sb_4S_{13}$) at a high Cu:Sb ratio.

The world is currently facing a serious energy crisis from high consumption of non-renewable fossil fuels. Therefore, there is currently a concerted drive towards developing green routes to produce sustainable energy from renewable sources, such as solar energy[1]. Photovoltaic (PV) devices have the potential to be low-cost and sustainable with high solar to electrical energy conversion efficiencies[2,3]. However, this is highly dependent on the abundance and cost of the initial materials and the scalability of the deposition technique.

Numerous metal chalcogenide materials such as copper selenide (CuSe), cadmium selenide (CdSe), copper indium sulfide /selenide (CIS/Se), copper tin telluride (CuSnTe), copper indium gallium sulfide/selenide (CIGS/Se), copper zinc tin sulfide (Cu_2ZnSnS_4) (CZTS), and copper iron tin sulfide (Cu_2FeSnS_4) have received attention as solar absorbers in photovoltaic cells in recent years[4–9]. Copper antimony sulfide ($CuSbS_2$)[10], copper antimony selenide sulfide ($CuSbSe_xS_{2-x}$)[11] and copper germanium selenide (Cu_2GeSe_3)[12] have recently been investigated as both nanoflakes and nanoparticles for electrochemical energy storage. Semiconducting copper and cadmium chalcogenides have played a significant role in developing high-efficiency solar cells. Copper indium gallium selenide (CuInGaSe) and cadmium telluride (CdTe) thin film solar cells have demonstrated efficiencies of 21.5% and 21.7%, respectively[13,14]. However, these materials have several disadvantages, such as

[1]Department of Materials, The University of Manchester, Oxford Road, Manchester M13 9PL, UK. [2]Department of Physics, College of Science, Jazan University, Jazan 82817, Saudi Arabia. [3]Department of Chemistry, The University of Manchester, Oxford Road, Manchester M13 9PL, UK. ✉email: david.lewis-4@manchester.ac.uk

low elemental abundance[15], high cost, and toxicity of elements such as Cd and Te[16]. These disadvantages have significantly hindered the widespread deployment of these materials as photovoltaic devices.

Ternary copper antimony sulfide has recently been proposed as an alternative PV material, due to the low-cost, earth-abundant, and non-toxic nature of the constituent elements[17]. Ternary copper antimony sulfide also yields high absorption coefficients (over 10^5 cm^{-1}) in several phases[18], with a suitable band gap for photovoltaic applications[10,19]. However, there are several distinct phases of copper antimony sulfide, (Cu-Sb-S) including Cu_3SbS_3 (skinnerite), $CuSbS_2$ (chalcostibite), $C_{12}Sb_4S_{13}$ (tetrahedrite), and Cu_3SbS_4 (fematinite)[20]. These materials all possess band gap energies between 1.1 and 1.9 eV, with high absorption coefficients ($> 10^5$ cm^{-1})[18], and are thus excellent candidates for solar energy harvesting[21–25]. However, phase-pure material of Cu-Sb-S (such as tetrahedrite) is difficult to achieve and has previously been reported as requiring several weeks and high temperatures for various melting and annealing steps[18,26,27]. Chalcostibite ($CuSbS_2$) in particular has been proposed as a candidate for the replacement of $CuInS_2$, due to equivalent optical properties and the natural abundance of antimony when compared to indium[18]. Tetrahedrite ($Cu_{12}Sb_4S_{13}$) is another important phase as this material is not only a good candidate for solar absorbance in photovoltaic devices[18], but also as a candidate for thermal energy harvesting as a thermoelectric device via the Seebeck effect[18].

The use of single-source precursors for the preparation of binary and ternary metal chalcogenides is of growing importance[18,28–31]. This method is potentially beneficial because of the simplicity, high purity, and tunable size of the produced materials[32]. Copper and antimony dithiocarbamate (DTC) complexes are frequently used for binary and ternary metal sulfide thin film preparation due to their ease of synthesis, clean decomposition at low temperature, and solubility of these complexes in many organic solvents[28,33–35]. Ternary copper-antimony sulfide nanocrystals have been previously prepared using single-source precursors of antimony diethyldithiocarbamate ($Sb(DTC)_3$) and copper diethyldithiocarbamate ($Cu(DTC)_2$)[36]. The produced copper antimony sulfide nanocrystals exhibit different compositions, band gaps, and morphologies including rhombic Cu_3SbS_3, rectangular $CuSbS_2$ nanosheets, and trigonal–pyramidal $Cu_{12}Sb_4S_{13}$ nanocrystals, which have shown promising potential for photovoltaic applications[37]. Zou *et. al.*, synthesized chalcostibite $CuSbS_2$ nanocrystals using a colloidal route with dodecanethiol as ligands. A direct band gap energy of 1.59 eV was reported, and they were further demonstrated to having utility in photovoltaic applications[38]. Regulacio *et. al.* used copper and antimony diethyldithiocarbamate precursors for the synthesis of high-purity tetrahedrite ($Cu_{12}Sb_4S_{13}$) nanostructures using solvothermal decomposition[39].

Numerous methods have been developed for the deposition of particulate, nanoscale and thin film copper antimony sulfides, such as the solvothermal[40], chemical bath deposition[41], spin coating[42], spray pyrolysis[43], thermal evaporation[44], and pulsed laser ablation[45]. Solventless thermolysis involves decomposition of a precursor under thermal stress. This method is inexpensive and is inherently more sustainable that most other methods due to the absence of solvent[46]. Solventless thermolysis also produces high yields for the synthesis of desired materials[18]. Different morphologies of metal chalcogenides can be prepared using this method such as nanorods[47], nanodisks[48], and cubic nanoparticles[49,50]. However, difficulty in controlling the size of particles in the presence of capping agents has limited progress in designing these nanomaterials[51].

In the present study, two facile, scalable, and cost-effective methods for the preparation of phase pure binary Sb_2S_3, Cu_2S and $Cu_{1.8}S$ are reported, and three distinct phases of ternary copper antimony sulfide ($CuSbS_2$, Cu_3SbS_4, and $Cu_{12}Sb_4S_{13}$) can be prepared as either particulates (using solventless thermolysis) or thin films (using AACVD). These materials are prepared from single-source precursors of copper and antimony diethyl-dithiocarbamates ($Cu(DTC)_2$ and $Sb(DTC)_3$) mixed at different molar ratios of Cu:Sb. The work presented here reports two simple and scalable routes towards several phases of ternary Cu-Sb-S, which are highly relevant for both photovoltaic and thermoelectric applications.

Experimental

Chemicals. All chemicals were purchased from Sigma Aldrich and used without further purification, unless specified. Sodium diethyldithiocarbamate trihydrate (($C_2H_5)_2NCS_2Na \cdot 3H_2O$, $\geq 99.0\%$), antimony trichloride ($SbCl_3$, $\geq 99.5\%$), anhydrous copper(II) chloride ($CuCl_2 \geq 98.0\%$), methanol (CH_3OH, $\geq 99.8\%$), absolute ethanol (CH_3CH_2OH, $\geq 99.5\%$), chloroform ($CHCl_3$, $\geq 99\%$) and isopropyl alcohol (($CH_3)_2CHOH$, $\geq 99.7\%$). Synthesis of the precursors was performed in air and no special handling or inert atmosphere was required.

Instrumentation. Elemental analysis (EA) was performed in the micro-analytical laboratory of the University of Manchester. Thermogravimetric analysis (TGA) was conducted using a Perkin Elmer TGA 4000, in a temperature range of 30 to 600 °C and a ramp rate of 10 °C min^{-1} under a nitrogen atmosphere. Powder XRD patterns were recorded using an XRD5-PANaytical X-Pert Pro theta-theta diffractometer (435 mm diameter). The data was collected using detector scans at a grazing incidence angle of 3° and were undertaken with a scan range of 5° to 85° with a 0.03° step at 8 s step^{-1}. Scanning electron microscopy (SEM) imaging was performed using an FEI Quanta 650 Field Emission GUN (FEG)-SEM equipped with an Oxford Instruments Xmax 50 Silicon Drift Detector (for EDX microanalysis) with an accelerating voltage of 10—20 kV. Raman spectra were recorded using a Renishaw 1000 Micro- Raman spectrometer, equipped with a 50×objective, with argon ion laser (514.5 nm, 25% powder).

Synthesis. *Copper diethyldithiocarbamate, Cu(DTC)₂ (1).* The synthesis of copper diethyldithiocarbamate ($Cu(DTC)_2$) was achieved by adapting a previously reported procedure[37]. Sodium diethyldithiocarbamate trihydrate (10 g, 44 mmol) was dissolved in 100 mL of methanol and stirred until fully dissolved. A separate solution of copper(II) chloride (2.89 g, 22 mmol) was prepared in 25 mL of methanol. The copper solution was then added dropwise to the diethyldithiocarbamate solution under constant stirring for 30 min. A black precipitate
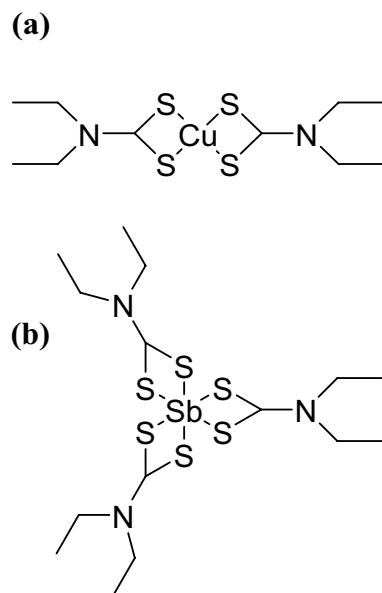
(a)

(b)

Figure 1. Figure showing the chemical structures of the two single-source precursors utilised in this report. These are (**a**) copper(II) diethyldithiocarbamate (Cu(DTC)$_2$) and (**b**) antimony(III) diethyldithiocarbamate (Sb(DTC)$_3$).

was formed, which was filtered, and washed three times with room temperature deionized water and methanol and dried overnight under atmospheric laboratory conditions. Yield 74%. Anal. found: C, 32.90%; H, 5.52%; N, 7.69%; S, 30.05%. Calc.: C, 33.37%; H, 5.61%; N, 7.79%; S, 35.56%. This could be due to some reduction of the Cu(II) to Cu(I), in line with previous reports[28,52] and our observations of chalcocite (Cu$_2$S, Fig. 8) and digenite (Cu$_{1.8}$S, Fig. 4). The chemical structure of the precursor is illustrated in Fig. 1a.

Antimony(III) diethyldithiocarbamate, Sb(DTC)$_3$ (2). The synthesis of antimony diethyldithiocarbamate (Sb(DTC)$_3$) was achieved by adapting a previously reported procedure[37]. Sodium diethyldithiocarbamate trihydrate (6.76 g, 30 mmol) was dissolved in 100 mL of methanol and stirred until fully dissolved. In a separate solution, antimony (III) chloride (2.26 g, 10 mmol) was dissolved in 25 mL of methanol. The prepared antimony chloride solution was then added dropwise to the diethyldithiocarbamate solution under constant stirring. Once fully added, the reaction mixture was further stirred for 30 min at room temperature. After this time, a yellow precipitate was filtered and washed several times with deionized water and methanol at room temperature. The product (yellow solid) was dried overnight at room temperature in atmospheric laboratory conditions. Yield 86%. Anal. found: C, 31.35%; H, 5.19%; N, 7.25%; S, 33.22%. Calc: C, 31.81%; H, 5.34%; N, 7.42%; S, 33.90%. The chemical structure of the precursor is illustrated in Fig. 1b.

Preparation of binary Cu$_x$S$_y$ and Sb$_2$S$_3$ powders by solventless thermolysis. Solventless thermolysis was used for the synthesis of particulate Cu$_x$S$_y$ and Sb$_2$S$_3$ using the single-source precursors Cu(DTC)$_2$ and Sb(DTC)$_3$, respectively. A measured amount (0.55 mmol) of precursor was placed into a ceramic boat inside a tube furnace and annealed at either 300, 400, 425, 450, or 475 °C for 1 h, under a nitrogen atmosphere. The obtained black product was cooled at room temperature and collected for characterization.

Preparation of copper-antimony-sulfide (Cu-Sb-S) powders by solventless thermolysis. Copper-antimony sulfide Cu$_{2x}$Sb$_{2(1-x)}$S$_y$ was prepared by solventless thermolysis using a mixture of both precursors (Cu(DTC)$_2$ and Sb(DTC)$_3$) at different molar ratios, where x = either 0, 0.2, 0.4, 0.6, 0.8 or 1 (the respective mol fractions, and absolute input amount (in mmol) are displayed in Table S1). The mixture was dissolved in 10 mL of chloroform to form a homogeneous solution. The solvent was then evaporated under kneading using a pestle and mortar. The obtained mixture was then placed into a ceramic boat and heated in a tube furnace at 450 °C for 1 h under a nitrogen atmosphere. The obtained black product was cooled at room temperature and collected for characterization.

Preparation of copper-antimony-sulfide (Cu-Sb-S) thin films by AACVD. Prior to deposition, glass slides of the dimensions 1 cm × 2.5 cm were thoroughly cleaned by consecutively washing with deionized water (DI) and acetone for 10 min each, under ultrasonic conditions. The glass slides were then dried in the oven before loading inside a reactor tube for deposition. The deposition of copper antimony sulfide thin films was carried out using the aerosol-assisted chemical vapor deposition (AACVD) technique. The different molar fractions of Cu(DTC)$_2$ and Sb(DTC)$_3$ were dissolved in 20 mL of tetrahydrofuran (THF) and transferred to a two-necked round bottom flask. The flask outlet was connected to the reactor tube via rubber tubing, and argon

gas was flowed into the inlet. The reactor tube was placed in a carbolite tube furnace and heated to 450 °C for one hour. The aerosol was generated by placing the reaction flask that contained the precursor solution on an ultrasonic aerosol generator. The argon flow (160–180 sccm) transported the aerosol to the hot wall reaction chamber where thermal decomposition took place to form a thin film on the substrates. The films obtained were then characterized by p-XRD, EDX, SEM, Raman, and UV–Vis spectroscopies.

Results and discussion

Solventless thermolysis of Cu(DTC)$_2$ and Sb(DTC)$_3$ to generate binary Cu$_x$S$_y$ and Sb$_2$S$_3$ systems.
The aim of this research is to generate target phases of Cu-Sb-S substrates through simple, cost-effective routes. Namely, investigating both solventless thermolysis and AACVD deposition techniques to decompose single-source precursors, producing both binary and ternary metal chalcogenides. Initially, the two single-source precursors (Cu(DTC)$_2$ and Sb(DTC)$_3$) were investigated individually for their thermal decomposition behaviour.

Thermogravimetric analysis (TGA) on the two single source precursors demonstrated that both these precursors decompose in the temperature range 240–340 °C. The Cu(DTC)$_2$ precursor observed a single, major decomposition with no further loss in mass with increasing temperature. The Sb(DTC)$_3$ precursor also observed a single step decomposition, but was followed by a more gradual decomposition at higher temperature, which is attributed to further loss of elemental sulfur[53]. The TGA results are shown in Fig. S1 and indicates that the two precursors decompose to their respective metal sulfides within a similar temperature range, this makes them ideal candidates to explore further to produce particulate binary metal chalcogenides.

Therefore, thermal decomposition (via solvent-less thermolysis) of the two precursors was performed to generate the respective binary particulate metal chalcogenide material. This was undertaken at a range of temperatures for 1 h. The crystallinity of the resultant particulate material was analysed by powder X-ray diffraction (p-XRD). The resultant p-XRD patterns of the particulate material generated from Sb(DTC)$_3$ at 300, 400, 425, 450, and 475 °C are shown in Fig. S2. This analysis revealed that the produced material was crystalline and corresponded to orthorhombic stibnite (Sb$_2$S$_3$, ICDD: 01-073-0393)[54] with lattice parameters a = 11.313 Å, b = 3.833 Å, and c = 11.225 Å.

Analysis of the particulate product of the Cu(DTC)$_2$ precursor, decomposed at 300, 350, 400, and 450 °C was also undertaken. The resulting p-XRD diffraction patterns of these particulate materials are shown in Fig. S3. Again, this analysis also showed that the resulting material was crystalline, with the major diffraction peaks corresponding to rhombohedral digenite (Cu$_{1.8}$S, ICDD 00-023-0962)[55] with minor peaks in the pattern corresponding to impurities of monoclinic chalcocite (Cu$_2$S, ICDD 00-033-0490, indicated by a * on the p-XRD spectra, Fig. S3)[56], which is particularly prevalent for reactions performed at lower temperatures. At higher decomposition temperatures (450 °C), there is no observable Cu$_2$S present, producing phase pure Cu$_{1.8}$S. The observed lattice parameters are a = 3.930 Å, b = 3.930 Å, and c = 48.650 Å, with the major diffraction peaks corresponding to the (015), (018), (101), (110), planes (as shown on Fig. S3). The morphology and elemental composition of these binary Cu$_{1.8}$S and Sb$_2$S$_3$ particulate materials were further investigated by SEM and EDX analysis, and are discussed later, together with the ternary Cu$_{2x}$Sb$_{2(1-x)}$S$_y$ systems.

Synthesis of ternary Cu$_{2x}$Sb$_{2(1-x)}$S$_y$ (0 ≤ x ≤ 1) powder by solventless thermolysis.
Following the success of producing particulate binary Cu$_{1.8}$S and Sb$_2$S$_3$ from their respective single-source precursors, the precursors were then investigated for their ability to synthesise the more complex ternary metal sulfides. The TGA analysis demonstrated that both precursors decompose to their corresponding metal sulfides in a similar temperature range. Both precursors are soluble in chloroform, toluene, and other organic solvents. Therefore, we concluded that these complexes are good candidates for decomposition in tandem to generate ternary metal sulfides[29], at lower temperatures and a faster time than typically employed for this synthesis (650 °C[26] and 3 weeks[27]).

These two precursors were therefore investigated towards the preparation of ternary copper-antimony-sulfide (Cu-Sb-S) material at various molar ratios of Cu:Sb. The temperature selected for this investigation was 450 °C, as this temperature produced the phase purest material in the Cu(DTC)$_2$ decomposition (Fig. S3). Therefore, solutions containing both precursors (Cu(DTC)$_2$ and Sb(DTC)$_3$) of various ratios (Table S1) were used to generate particulate Cu$_{2x}$Sb$_{2(1-x)}$S$_y$ material, where the mol fraction (x) used was 0 (*i.e.* only Sb$_2$S$_3$), 0.2, 0.4, 0.6, 0.8 and 1 (*i.e.* only Cu$_{1.8}$S).

SEM and EDX analysis of particulate Cu$_{1.8}$S, Sb$_2$S$_3$, and Cu$_{2x}$Sb$_{2(1-x)}$S$_y$ generated by solventless thermolysis.
Initially, SEM and EDX spectroscopies were used to study the morphology and elemental composition of the generated particulate Cu$_{2x}$Sb$_{2(1-x)}$S$_y$ material, at various values of x. Representative SEM images of the six Cu$_{2x}$Sb$_{2(1-x)}$S$_y$ systems, where x = 0, 0.2, 0.4, 0.6, 0.8 and 1 are shown in Fig. 2. SEM analysis of pure Sb$_2$S$_3$ (x = 0) revealed micro-rod structures (Fig. 2a), which are consistent with previously reported particulate Sb$_2$S$_3$, prepared using hydrothermal decomposition of an antimony diethyldithiocarbamate precursor[34]. As the Cu content of the systems increased, the morphology changed to a mixture of shorter-length micro-rods and agglomerated clusters at x = 0.2, as shown in Fig. 2b. As the Cu content increased to x = 0.4, again both rods and clusters are present, as shown in Fig. 2c. Increasing the molar fraction of Cu to x = 0.6 and x = 0.8 showed no rod-character and only cluster-character (Fig. 2d and e). Finally, the morphology of pure Cu$_{1.8}$S, where x = 1, showed even further (and smaller scale) clustering, resembling a floret-like morphology (Fig. 2f).

These six particulate samples were then assessed for elemental composition by EDX spectroscopy. The Cu$_{2x}$Sb$_{2(1-x)}$S$_y$ systems where x = 0.2, 0.4, 0.6, and 0.8 showed the characteristic peaks of copper, antimony, and sulfur (Fig. S4). Figure S5 shows both the expected elemental composition and the observed experimental
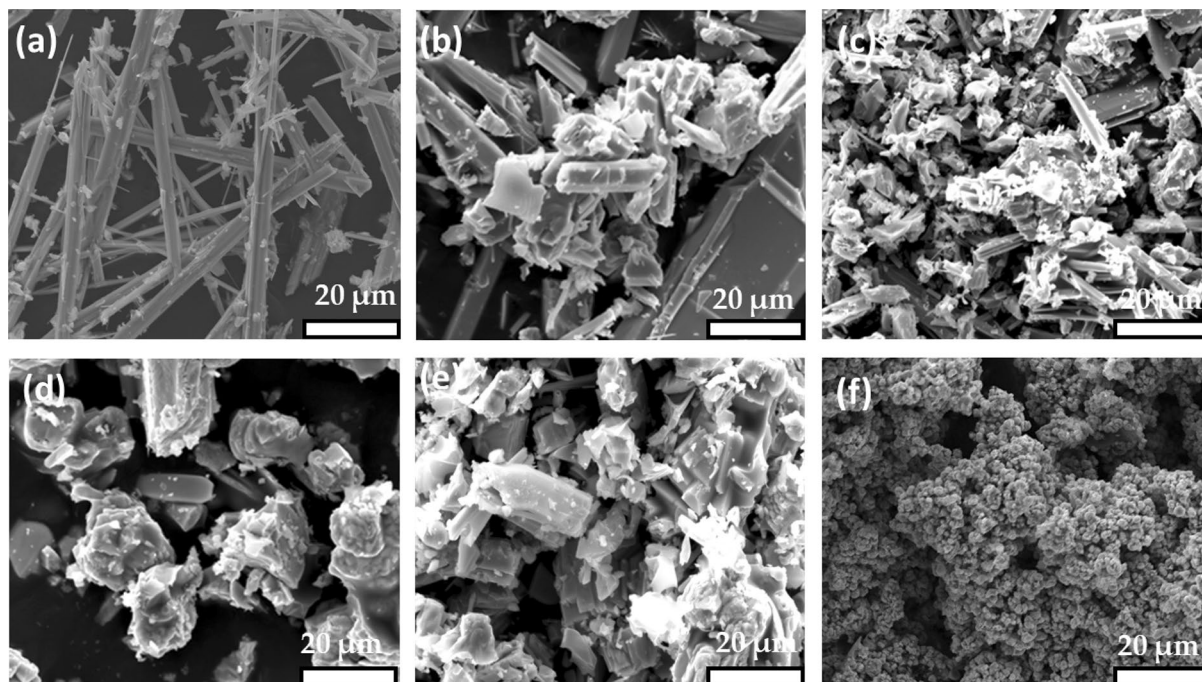
Figure 2. Representative SEM images of particulate $Cu_{2x}Sb_{2(1-x)}S_y$ prepared by solventless thermolysis at 450 °C for 1 h where x = (**a**) 0, (**b**) 0.2, (**c**) 0.4, (**d**) 0.6, (**e**) 0.8 and (**f**) 1. These were recorded at 15 k eV using secondary electron SEM.

composition for both Cu and Sb, based on the EDX analysis, the data is also tabulated in Table S2. As shown in Fig. S5, the linear relationship between the expected and observed Cu and Sb mol% of the various synthesised particulate $Cu_{2x}Sb_{2(1-x)}S_y$ systems are in good agreement, with both observing a > 98% fit). The one outlier is the Cu and Sb composition in the x = 0.6 system, which is deficient in Cu and rich in Sb (Table S2).

EDX spectroscopic mapping of $Cu_{2x}Sb_{2(1-x)}S_y$. EDX elemental mapping was performed on the four $Cu_{2x}Sb_{2(1-x)}S_y$ systems where 0 < x < 1. This was not performed where x = either 0 or 1, as pXRD analysis above already demonstrated no contamination of Sb in the x = 1 system or Cu in the x = 0 system. The resultant element maps are shown in Fig. 3, which show the spatial distribution of Cu, Sb and S. From this analysis it is clear that the Cu and Sb are predominantly co-localised, which suggests formation of the ternary metal sulfide material, as opposed to two separate phases of Cu_xS_y and Sb_xS_y. However, we do note apparent Cu-rich areas in the material where x = 0.2 (Fig. 3a) which suggests some limited phase separation. Despite this, there is strong evidence of the presence of alloyed $Cu_{2x}Sb_{2(1-x)}S_y$.

This analysis yields useful insight into the generated particulate $Cu_{2x}Sb_{2(1-x)}S_y$ material, but does not indicate whether these structures are crystalline, or the phase or absolute composition of these particulate systems. To investigate this further, powder X-ray diffraction was employed on all six synthesised $Cu_{2x}Sb_{2(1-x)}S_y$ systems.

Powder X-ray diffraction analysis of $Cu_{2x}Sb_{2(1-x)}S_y$. With the SEM analysis showing a change in morphology with increasing Cu character in the particulate $Cu_{2x}Sb_{2(1-x)}S_y$ systems, and the EDX elemental mapping analysis showing the presence of both Cu and Sb localised together, these six particulate systems were investigated by powder XRD to determine both the crystallinity and the phase of the various $Cu_{2x}Sb_{2(1-x)}S_y$ systems produced.

The p-XRD spectra of the six particulate $Cu_{2x}Sb_{2(1-x)}S_y$ systems are shown in Fig. 4. As previously discussed, the XRD pattern for the sample where x = 0 could be indexed to orthorhombic stibnite (Sb_2S_3), and the XRD pattern for x = 1 could be indexed to rhombohedral digenite ($Cu_{1.8}S$). Next, the samples where 0 < x < 1 were analysed. For the sample where x = 0.2, XRD showed peaks consistent with ternary chalcostibite ($CuSbS_2$), with impurities of Sb_2S_3. Increasing the mole fraction to x = 0.4 resulted in the formation of orthorhombic chalcostibite ($CuSbS_2$, ICDD: 00-044-1417) (Fig. 4b). Upon further increasing the molar ratio of Cu to x = 0.6, a different phase of ternary copper antimony sulfide was observed; tetrahedrite ($Cu_{12}Sb_4S_{13}$, ICDD: 01-074-0270), with lattice parameters of a = 11.423 Å, b = 14.174 Å, and c = 3.765 Å, with some impurities of $Cu_{1.8}S$. Previous reports have demonstrated that it is difficult to avoid a small number of impurities in the synthesis of tetrahedrite[57,58], particularly when using copper and antimony xanthate (dithiocarbonate) precursors[18]. The presence of these impurities also account for the slight discrepancy in the EDX elemental composition analysis. Finally, increasing the molar ratio of Cu to x = 0.8 resulted in the generation of predominantly pure phase cubic tetrahedrite ($Cu_{12}Sb_4S_3$, ICDD: 01-074-0270), as shown by the XRD pattern in Fig. 4c.
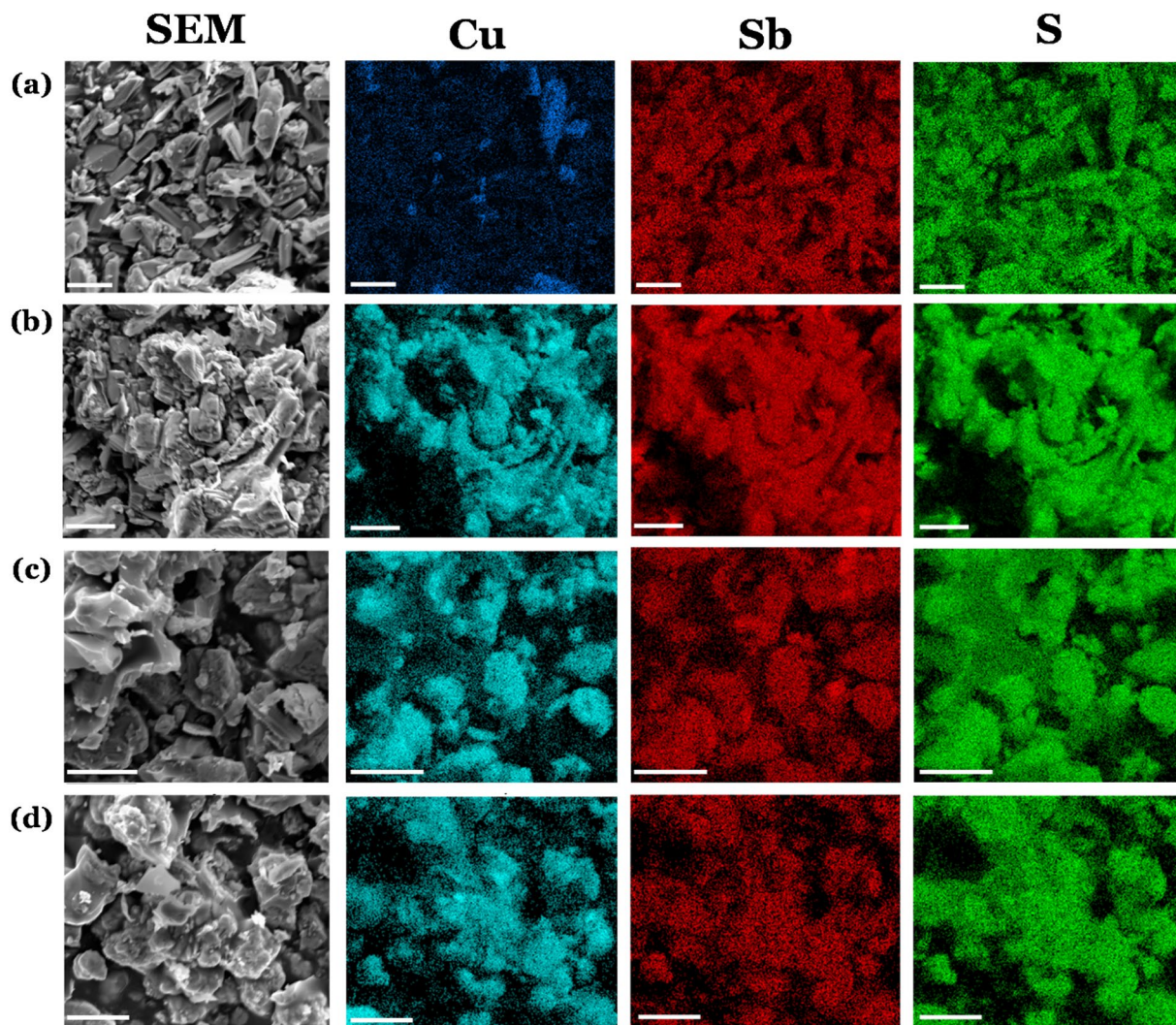
Figure 3. EDX elemental mapping analysis of the various particulate $Cu_{2x}Sb_{2(1-x)}S_y$ systems prepared by solventless thermolysis at 450 °C for 1 h, where x = (**a**) 0.2, (**b**) 0.4, (**c**) 0.6 and (**d**) 0.8. Elemental mapping is also shown for (green) sulfur (Kα), (blue) copper (Kα) and (red) antimony (Lα). These were recorded at 15 k eV using secondary electron SEM. All scale bars presented correspond to 10 μm.

Raman Spectroscopy of the $Cu_{2x}Sb_{2(1-x)}S_y$ systems. Raman spectroscopy was used to further study the particulate binary $Cu_{1.8}S$ and Sb_2S_3 and ternary $Cu_{2x}Sb_{2(1-x)}S_y$ systems (as shown in Fig. 5). The three systems where x = 0, 0.2 and 1 are shown in Fig. S6. For the system where x = 0.4, Raman spectroscopy further confirms the presence of pure chalcostibite ($CuSbS_2$), with a sharp peak at 332 cm^{-1}, and lower intensity peak at 250 cm^{-1} [18]. The p-XRD analysis indicates that the x = 0.6 and 0.8 systems were both tetrahedrite, of varying purities (Fig. 4). The Raman spectra of these systems displayed a sharp peak at 350 cm^{-1}, corresponding to cubic tetrahedrite $Cu_{12}Sb_4S_{13}$ [18]. In the x = 0.6 system, a further peak at 250 cm^{-1} is also observed, which corresponds to Cu–S bonding (from the $Cu_{1.8}S$ impurity) [59–61]. This peak reduces in intensity as the mol fraction of Cu increases. These results correlate well with those previously reported for chalcostibite and tetrahedrite, obtained by solventless thermolysis of xanthate precursors of Cu and Sb [18].

AACVD of $Cu_{2x}Sb_{2(1-x)}S_y$ (0 ≤ x ≤ 1) thin film systems. Having successfully synthesised particulate material of binary $Cu_{1.8}S$ and Sb_2S_3, and ternary $CuSbS_2$ and $Cu_{12}Sb_4S_{13}$, by simply altering the ratio of Cu: Sb precursors using solventless thermolysis, we next set out to produce thin films of these materials. For this, aerosol-assisted chemical vapor deposition (AACVD) was utilised. AACVD is a ubiquitous and widely employed method of generating films of metal chalcogenide materials from both metal dithiocarbamate and metal xanthate single-source precursors [28,62–64]. This technique was therefore utilised here to deposit both binary and ternary metal sulfides.

Deposition of Sb_2S_3, Cu_9S_5 and $Cu_{2x}Sb_{2(1-x)}S_y$ by AACVD onto glass substrates was performed using a method described previously [65]. The aerosol was generated by an ultrasonic humidifier and transported by flowing argon. Deposition of the films was carried out for 1 h at 450 °C, which generated matte black films with good surface
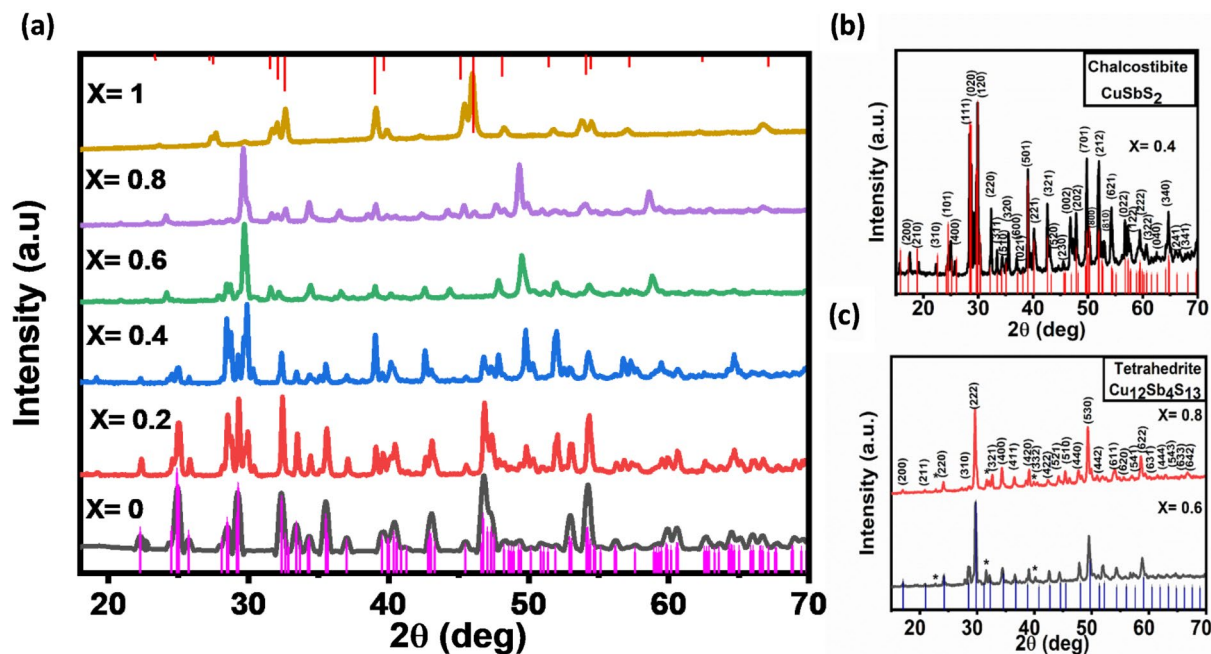
Figure 4. Plots showing the p-XRD analysis of $Cu_{2x}Sb_{2(1-x)}S_y$ produced by solventless thermolysis at 450 °C, where the mole fraction of Cu:Sb (x) was altered as in (**a**) x = 0, 0.2, 0.4, 0.6, 0.8 and 1, where x = 0 produced pure Sb_2S_3 (ICDD: 01-073-0393, stick pattern at bottom) and x = 1 produced pure $Cu_{1.8}S$ (ICDD 00-023-0962, stick pattern at top). Also shown are the individual p-XRD patterns for (**b**) x = 0.4, showing pure chalcostibite ($CuSbS_2$, ICDD: 00-044-1417) and (**c**) x = 0.6 and 0.8, showing pure tetrahedrite $Cu_{12}Sb_4S_{13}$ (ICDD: 01-074-0270).
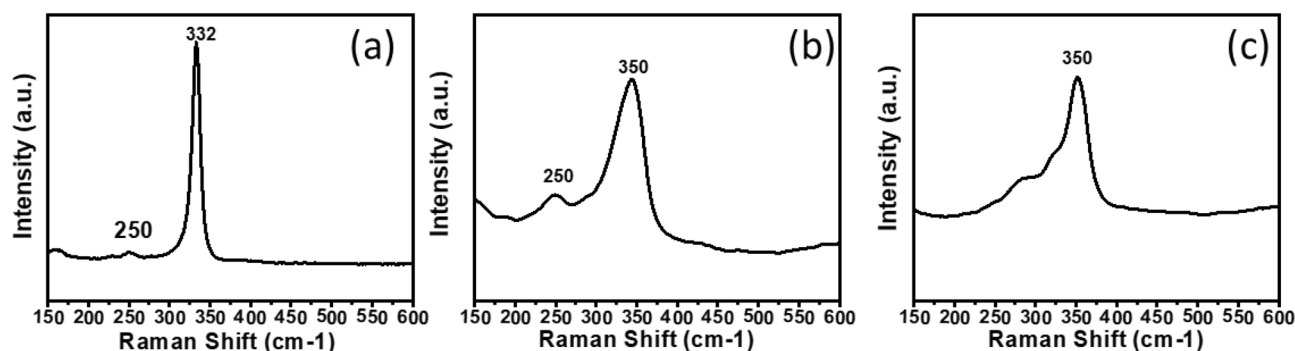

Figure 5. Raman spectra of the particulate $Cu_{2x}Sb_{2(1-x)}S_y$ systems where x = (**a**) 0.4, (**b**) 0.6 and (**c**) 0.8. Indicating the presence of chalostibite ($CuSbS_2$) and tetrahedrite ($Cu_{12}Sb_4S_{13}$), respectively.

coverage, as in Fig. S7. Initially, the morphology and elemental composition analysis was conducted on these six sample films by SEM and EDX spectroscopy.

SEM, EDX and Elemental mapping analysis of the $Cu_{2x}Sb_{2(1-x)}S_y$ thin films.
The surface morphology of binary and ternary copper antimony sulfide thin films were initially investigated by SEM. Figure 6 shows representative SEM images of the six investigated films. When x = 0 (*i.e.* when only Sb is present), and x = 0.2, the SEM images again show rod-shaped structures (Fig. 6a,b). Upon increasing x to 0.4, the morphology changed to spherical particles rather than rods, which are also observed upon further increasing x to 0.6 and 0.8 (Fig. 6c–e). Chalapathi *et. al.* has previously reported that thin films of Cu_3SbS_4, generated by chemical bath deposition have a spherical crystal morphology[66]. Van Ebden *et. al.* has also reported spherical nanoparticles of tetrahedrite ($Cu_{12}Sb_4S_{13}$)[23]. Therefore, our morphological analysis is in some agreement with the prior literature, despite being different from the particulate material generated by solventless thermolysis (Fig. 2). Finally, when x = 1 (*i.e.* only Cu is present), flake-like sheets were observed (Fig. 6f), which is consistent with a previous report of AACVD decomposition of a bis[N,N-dipropyl-N-(1-naphthoyl)thioureato]copper(II) precursor[67].

Following the morphological investigation of the thin film $Cu_{2x}Sb_{2(1-x)}S_y$ samples, elemental composition analysis was then investigated through EDX spectrscopy and is summarised in Table S3 (spectra are shown in
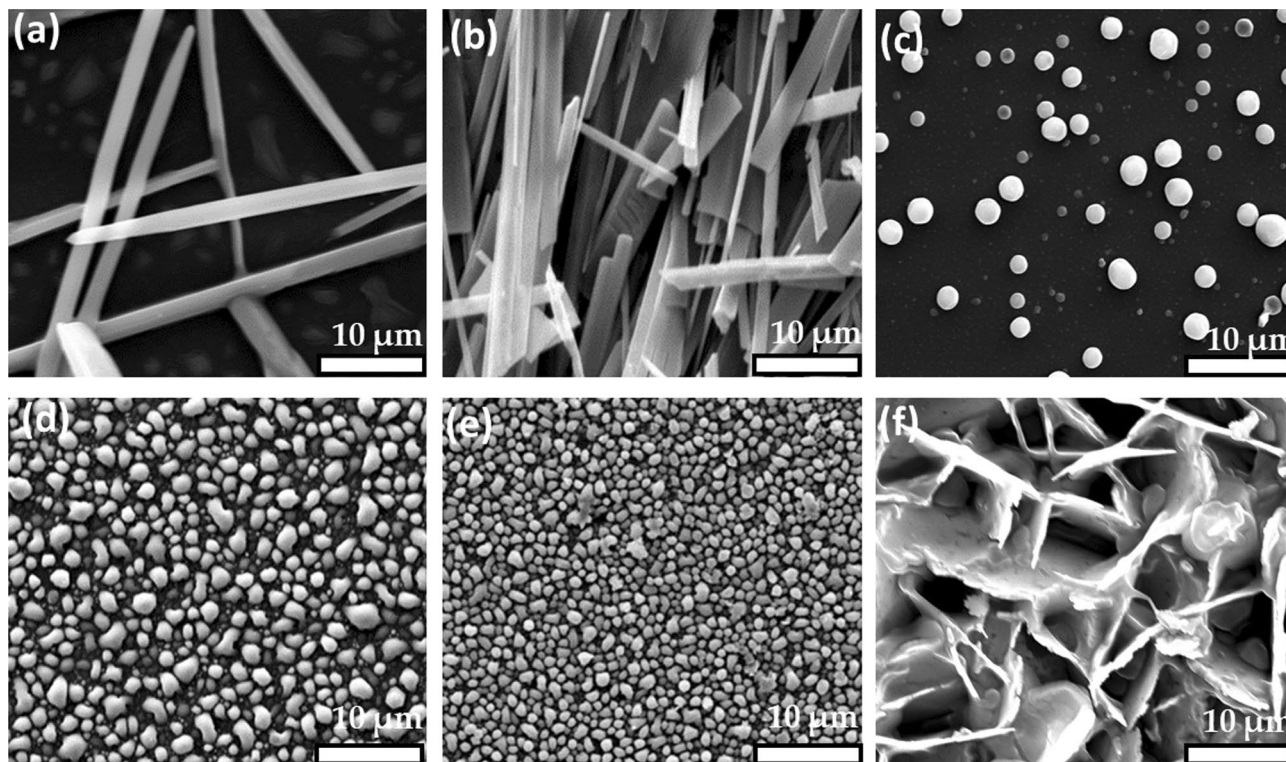
Figure 6. Representative SEM images of $Cu_{2x}Sb_{2(1-x)}S_y$ thin film synthesised by the hot-wall AACVD at 450 °C using various values of x, where x = (**a**) 0, (**b**) 0.2, (**c**) 0.4, (**d**) 0.6, (**e**) 0.8 and (**f**) 1. These were recorded at 15 k eV using secondary electron SEM.

Fig. S8). For the binary systems where x = 0 only Sb and S were present in the expected ratio (*ca.* 45:55), and x = 1 only Cu and S were present, also in the expected ratio (*ca.* 65:35).

For the ternary systems where 0 < x < 1, a composition of both Sb and Cu were present, alongside S. The ternary systems where x = 0.4, 0.6 and 0.8 all have the expected composition (Table S3). The system where x = 0.2 was found to be Sb-rich and S-deficient, which could again be due to the presence of impurities. Comparison of the EDX analysed expected *vs* observed Cu and Sb content again found a linear correlation (Fig. S9), equal to the particulate $Cu_{2x}Sb_{2(1-x)}S_y$ samples generated by solventless thermolysis. We note a linear correlation between the observed Cu and Sb to that expected when considering the phases of the Cu-Sb-S produced and identified by pXRD (vide infra).

Having investigated the surface morphology of the deposited thin films, the $Cu_{2x}Sb_{2(1-x)}S_y$ thin films were investigated using EDX spectroscopic elemental mapping on the samples where 0 < x < 1. This analysis visualizes the distribution of all constituent elements (Cu, Sb and S) within the films (Fig. 7). The materials deposited by AACVD demonstrate some Cu-rich areas in the film where x = 0.2 (Fig. 7a). As can also be observed, these Cu-rich areas are also Sb-deficient relative the rest of the material. This analysis indicates that the two binary Cu–S and Sb-S phases were deposited separately, rather than depositing any ternary Cu-Sb-S material. This outcome is supported by the p-XRD analysis (vide infra) which could not accurately determine any distinct ternary phase. In the x = 0.4 thin film, there also appears to be Sb-rich areas (the larger particles in Fig. 7b). This is due to the presence of Sb_2S_3 impurities as also shown by the pXRD pattern (Fig. 8).

Powder XRD analysis of the $Cu_{2x}Sb_{2(1-x)}S_y$ thin films. The SEM, EDX spectroscopy and elemental mapping of the various $Cu_{2x}Sb_{2(1-x)}S_y$ thin films showed that the Cu and Sb are on the whole spatially localised. However, the morphology of these materials was different to those obtained through solventless thermolysis, therefore the thin films were further investigated through powder XRD, to determine the phase of each material.

All deposited thin films where x < 1 displayed sharp peaks in their p-XRD patterns, indicating some crystallinity throughout the film. The deposited film where x = 0 (*i.e.* Sb only) could again be indexed to orthorhombic Sb_2S_3 (ICDD: 01-071-2432) with respective lattice parameters of a = 11.2902 b = 3.6953 Å and c = 11.1398 Å; α = β = γ = 90°, which is equivalent to the antimony sulfide generated through solventless thermolysis. As the concentration of Cu increased at x = 0.2, the p-XRD pattern remained that of orthorhombic Sb_2S_3, with some further peaks at higher 2θ, which could not be attributed to any products. At x = 0.4, a majority of tetragonal fematinite (Cu_3SbS_4, ICDD: 01-071-0555) is observed, with lattice parameters a = 5.3740 Å, b = 5.37540 Å & c = 10.5340 Å (Fig. 8b). Impurities that we attribute to Sb_2S_3 are also observed and are marked by an * in Fig. 8b. Notably, this is a different phase of copper-antimony-sulfide to that obtained from the solventless thermolysis deposition at the same mole ratio of Cu:Sb. These different phases in the x = 0.2 and 0.4 systems deposited by
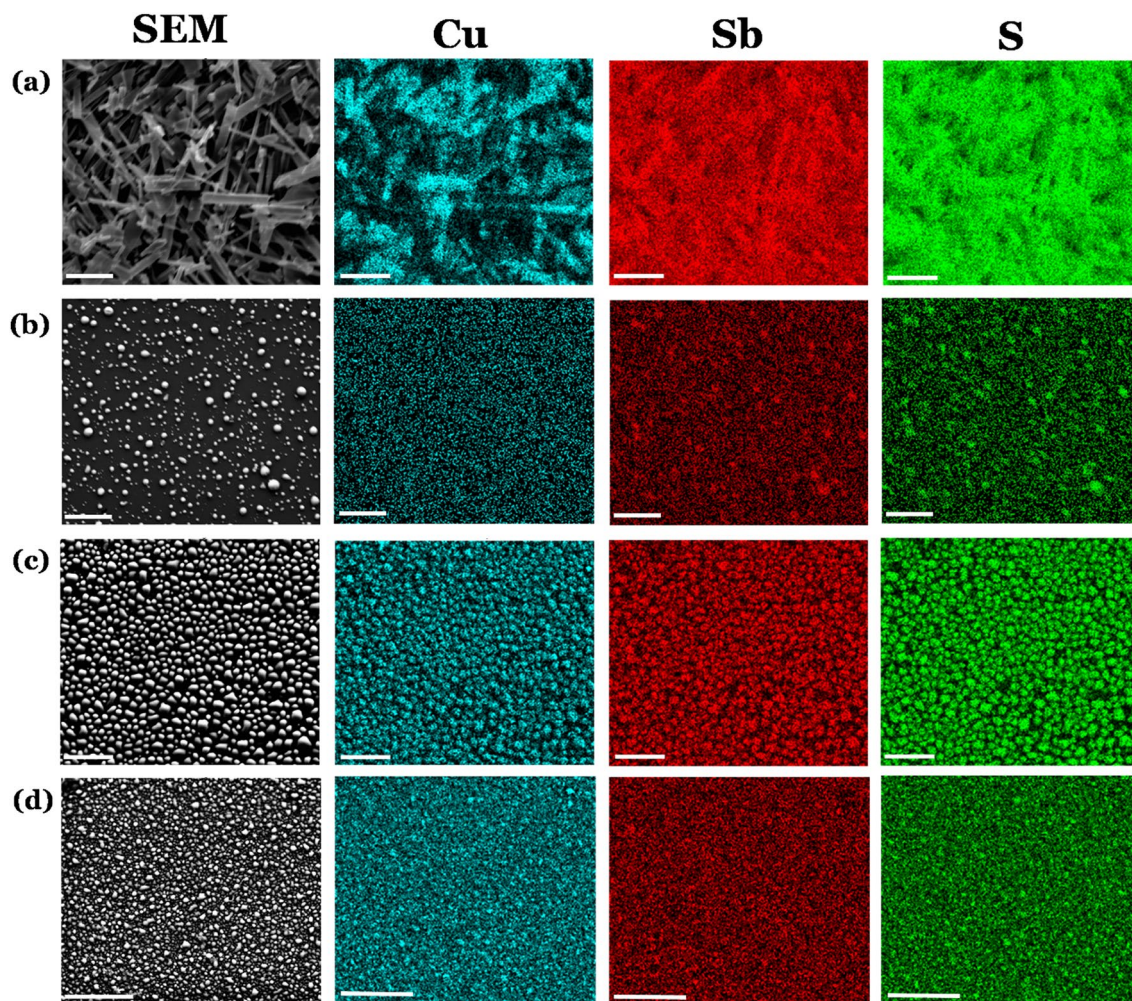
Figure 7. Figure showing both SEM (column 1) and elemental analysis maps (column 2, 3 and 4) for the four $Cu_{2x}Sb_{2(1-x)}S_y$ systems where (**a**) x = 0.2, (**b**) x = 0.4, (**c**) x = 0.6 and (**d**) x = 0.8. These films were deposited by AACVD and decomposed at 450 °C. Elemental mapping is also shown for (green) sulfur (Kα), (blue) copper (Kα) and (red) antimony (Lα). These were recorded at 15 k eV using secondary electron SEM. Scale bars correspond to 10 μm.

either AACVD to solventless thermolysis was compared to the phase diagram for Cu-Sb-S at 500 °C[68]. It has been reported that the thermodynamic product at the two Cu:Sb:S ratios where x = 0.2 and 0.4 (assuming 100% reduction of Cu(ii) to Cu(i)) are chalcosibite (CuSbS$_2$). Therefore, the formation of stibnite (Sb$_2$S$_3$) and fematinite (Cu$_3$SbS$_4$) demonstrates that AACVD deposition can form kinetic products. We note that solventless thermolysis forms the thermodynamically favourable digenite (C$_{1.8}$S) and AACVD deposits the kinetic chalcocite (Cu$_2$S)[68].

At x = 0.6 and 0.8, the phase produced is cubic tetrahedrite (Cu$_{12}$Sb$_4$S$_{13}$ ICDD: 01-088-0283) with lattice parameters a = b = c = 10.2853 Å (Fig. 8c), which is consistent with the $Cu_{2x}Sb_{2(1-x)}S_y$ material obtained from solventless thermolysis. The XRD pattern of the x = 1 thin film has sharp peaks. These peaks can be indexed to cubic Cu$_2$S (ICDD: 01-084-1770) with lattice parameters equal to a = b = c = 5.4539 Å. This is again different to the equivalent solventless thermolysis deposition which produced Cu$_{1.8}$S, perhaps indicating less sulfur loss is observed using AACVD and that AACVD in this case is prone to deposit a kinetic, rather than the thermodynamically favourable phase[68].

Raman spectroscopy of the $Cu_{2x}Sb_{2(1-x)}S_y$ thin films.   Following the successful characterisation of the phases of the AACVD deposited $Cu_{2x}Sb_{2(1-x)}S_y$ thin films, the films were analysed by Raman spectroscopy. The Raman spectra for the films where x = 0, 0.2 and 1 are shown in Fig. S10. For the thin film deposited when x = 0.4, the peaks in the Raman spectrum appear at 253, 273, 317 and 343 cm^{-1} (Fig. 9a), which correspond to tetragonal famatinite Cu$_3$SbS$_4$[69], confirming the p-XRD characterisation. As x was increased to 0.6 and 0.8, the Raman peak was shifted to 352 cm^{-1}, which correspond to cubic tetrahedrite Cu$_{12}$Sb$_4$S$_{13}$[59,60] (Fig. 9b). A further peak at 323 cm^{-1} was observed in the x = 0.8 thin film, also indicating pure cubic tetrahedrite Cu$_{12}$Sb$_4$S$_{13}$ (Fig. 9c). These results are agreement with the previous literature investigating various phases of copper-antimony-sulfur[18].
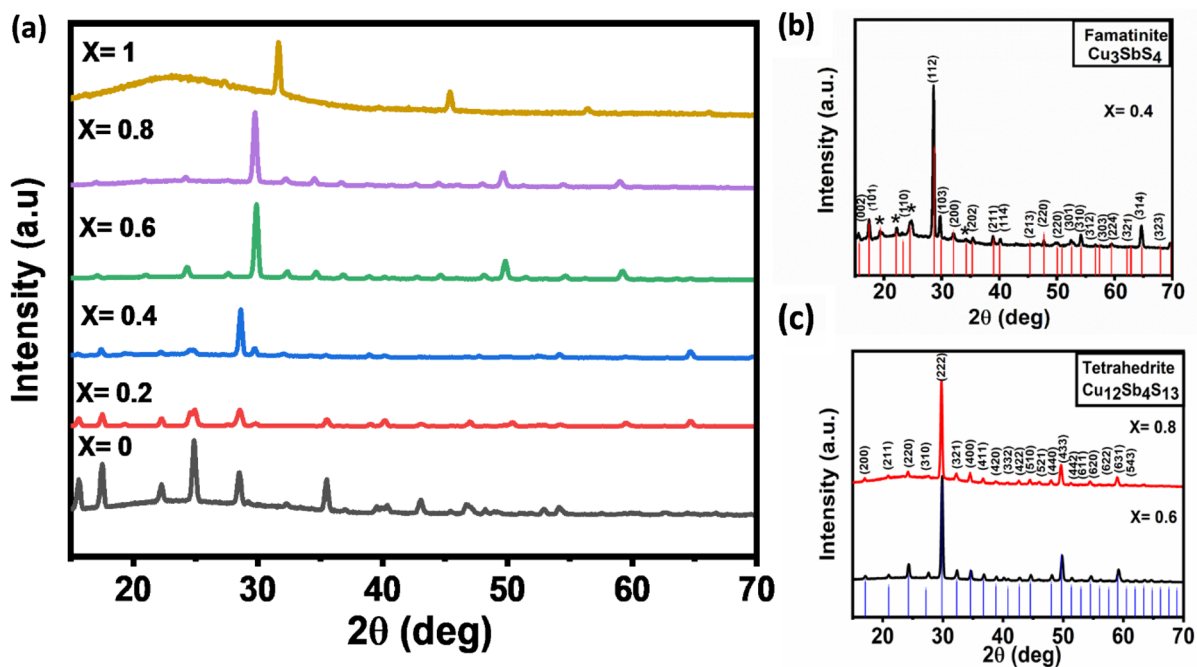
Figure 8. Plots showing the powder-XRD patterns for (**a**) all deposited $Cu_{2x}Sb_{2(1-x)}S_y$ thin films of x = 0, 0.2, 0.4, 0.6, 0.8 and 1. Also shown are the individual patterns for (**b**) x = 0.4 fematinite (Cu_3SbS_4, ICDD: 01-071-0555) and (**c**) x = 0.6 and x = 0.8 tetrahedrite ($Cu_{12}Sb_4S_{13}$, ICDD:01-088-0283). These spectra were recorded on the AACVD thin films, deposited at 450 °C.
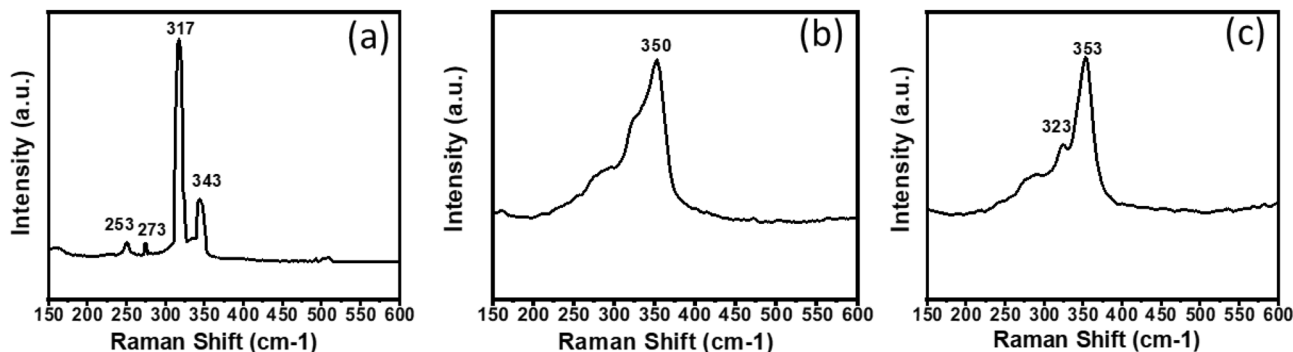

Figure 9. Raman spectra recorded for the AACVD-deposited thin films of $Cu_{2x}Sb_{2(1-x)}S_y$ where x = (**a**) 0.4 (**b**) 0.6 and (**c**) 0.8. Indicating the presence of (**a**) famatinite (Cu_3SbS_4) and (**b**) and (**c**) tetrahedrite ($Cu_{12}Sb_4S_{13}$).

Conclusions

In this study, binary and ternary Cu-Sb-S phases were produced by the thermal decomposition of both copper and antimony diethyldithiocarbamate single source precursors. We produced particulates and thin films through solventless thermolysis, or aerosol-assisted chemical vapor deposition, respectively. Utilising different methods of deposition resulted in the generation of different phases when altering the ratio of Cu:Sb precursors. Under solventless thermolysis using a low Cu ratio produced chalcostibite ($CuSbS_2$), and digenite ($Cu_{1.8}S$) with no Sb precursor present. Using AACVD to deposit thin films resulted in the formation of fematinite (Cu_3SbS_4) under a low Cu ratio and chalcocite (Cu_2S) with no Sb precursor present. Both methods were found to produce stibnite (Sb_2S_3) with no Cu present and tetrahedrite ($Cu_{12}Sb_4S_{13}$) with a high ratio of Cu:Sb.

The morphology of these produced materials was characterised by SEM and the elemental composition of these materials was determined through EDX analysis and EDX-mapping. These analyses demonstrated that the morphology of the materials change from a rod-like structure at low Cu content to more particulate material with increasing Cu content. Elemental mapping demonstrated that Cu and Sb were present in the same local environments, indicating the successful synthesis of ternary metal sulfides, which was confirmed by powder XRD and Raman spectroscopy.

This report demonstrates that both deposition methods (solventless thermolysis and AACVD) provide a facile, low-temperature and efficient synthetic approach towards the preparation of phase pure binary and ternary

metal sulfides from single-source diethyldithiocarbamate precursors. The synthesised phase-pure ternary copper antimony sulfide materials CuSbS$_2$, Cu$_3$SbS$_4$ and Cu$_{12}$Sb$_4$S$_{13}$ are all targets relevant for photovoltaic applications, and it is likely this approach is universal towards the synthesis of ternary metal chalcogenides.

References

1. Bahrampour, H., Beheshti, M. A. K., Askari, M. B. & Bahrampour, M. R. Evaluation of renewable energies production potential in the Middle East: Confronting the world's energy crisis. *Front. Energy* **14**, 42–56 (2020).
2. Blanco, C. F., Cucurachi, S., Peijnenburg, W. J. G. M., Beames, A. & Vijver, M. G. Are technological developments improving the environmental sustainability of photovoltaic electricity?. *Energy Technol.* **8**, 50 (2020).
3. Seri, M. *et al.* Toward real setting applications of organic and perovskite solar cells: A comparative review. *Energy Technol.* **9**, 10 (2021).
4. Ansari, M. Z. & Khare, N. Effect of intrinsic strain on the optical band gap of single phase nanostructured Cu2ZnSnS4. *Mater. Sci. Semicond. Process.* **63**, 220–226 (2017).
5. Thiruvenkadam, S., Jovina, D. & Leo, R. A. The influence of deposition temperature in the photovoltaic properties of spray deposited CZTS thin films. *Sol. Energy* **106**, 166–170 (2014).
6. Nagaura, T. *et al.* Universal electrochemical synthesis of mesoporous chalcogenide semiconductors: Mesoporous CdSe and CdTe thin films for optoelectronic applications. *Angew. Chemie - Int. Ed.* **60**, 9660–9665 (2021).
7. Kim, Y. *et al.* Atomic-layer-deposition-based 2D transition metal chalcogenides: Synthesis, modulation, and applications. *Adv. Mater.* **2005907**, 1–33 (2021).
8. Madhusudanan, S. P., Suresh, K. M., Mohanta, K. & Batabyal, S. K. Photoactive Cu2FeSnS4 thin films: Influence of stabilizers. *Appl. Surf. Sci.* **535**, 1005 (2021).
9. Wong, L. H., Zakutayev, A., Major, J. D., Hao, X. & Walsh, A. Emerging inorganic solar cell efficiency tables. *J. Phys. Energy* **1**, 032001 (2019).
10. Ramasamy, K. *et al.* Layered ternary sulfide CuSbS2 nanoplates for flexible solid-state supercapacitors. *J. Mater. Chem. A* **3**, 13263–13274 (2015).
11. Ramasamy, K., Gupta, R. K., Palchoudhury, S., Ivanov, S. & Gupta, A. Layer-structured copper antimony chalcogenides (CuSb-SexS2-x): Stable electrode materials for supercapacitors. *Chem. Mater.* **27**, 379–386 (2015).
12. Ganesan, V. & Kim, J. Shape effect on electrochemical energy storage performance of nanosized copper germanium selenide particles. *Bull. Korean Chem. Soc.* **42**, 641–644 (2021).
13. Banu, S., Ahn, S. J., Ahn, S. K., Yoon, K. & Cho, A. Fabrication and characterization of cost-efficient CuSbS2 thin film solar cells using hybrid inks. *Sol. Energy Mater. Sol. Cells* **151**, 14–23 (2016).
14. Gutierrez, Z. B. K. *et al.* CdS/CdTe heterostructures for applications in ultra-thin solar cells. *Materials (Basel).* **11**, 2–9 (2018).
15. Ramanujam, J. & Singh, U. P. Copper indium gallium selenide based solar cells-A review. *Energy Environ. Sci.* **10**, 1306–1319 (2017).
16. Kumar, B. H., Shaji, S. & Kumar, M. C. S. Effect of substrate temperature on properties of co-evaporated copper antimony sulfide thin films. *Thin Solid Films* **697**, 1007 (2020).
17. Ornelas-Acosta, R. E. *et al.* Thin films of copper antimony sulfide: A photovoltaic absorber material. *Sci. Rep.* https://doi.org/10.1016/j.materresbull.2014.10.027 (2015).
18. Alqahtani, T., Khan, M. D., Lewis, D. J., Zhong, X. L. & O'Brien, P. Scalable synthesis of Cu–Sb–S phases from reactive melts of metal xanthates and effect of cationic manipulation on structural and optical properties. *Sci. Rep.* **11**, 1–18 (2021).
19. Tiwari, K. J., Vinod, V., Subrahmanyam, A. & Malar, P. Growth and characterization of chalcostibite CuSbSe 2 thin films for photovoltaic application. *Appl. Surf. Sci.* https://doi.org/10.1016/j.apsusc.2017.01.279 (2017).
20. Suehiro, S. *et al.* Synthesis of copper-antimony-sulfide nanocrystals for solution-processed solar cells. *Inorg. Chem.* https://doi.org/10.1021/acs.inorgchem.5b00858 (2015).
21. Garza, C. *et al.* P-Type CuSbS2 thin films by thermal diffusion of copper into Sb2S3. *Sol. Energy Mater. Sol. Cells* **95**, 2001–2005 (2011).
22. Rodriguez-Lazcano, Y., Nair, M. T. S. & Nair, P. K. Cu x Sb y S z thin films produced by annealing chemically deposited Sb 2 S 3-CuS thin films. *Modern Phys. Lett. B* **15**, 1259 (2001).
23. Van Embden, J., Latham, K., Duffy, N. W. & Tachibana, Y. Near-infrared absorbing Cu12Sb4S13 and Cu3SbS4 nanocrystals: Synthesis, characterization, and photoelectrochemistry. *J. Am. Chem. Soc.* **135**, 11562–11571 (2013).
24. Ramasamy, K., Sims, H., Butler, W. H. & Gupta, A. Selective nanocrystal synthesis and calculated electronic structure of all four phases of copper-antimony-sulfide. *Chem. Mater.* **26**, 2891–2899 (2014).
25. Liu, Y. *et al.* Bandgap aligned Cu 12 Sb 4 S 13 quantum dots as efficient inorganic hole transport materials in planar perovskite solar cells with enhanced stability. *Sustain. Energy Fuels* **3**, 831–840 (2019).
26. Lu, X., Morelli, D. T., Xia, Y. & Ozolins, V. Increasing the thermoelectric figure of merit of tetrahedrites by Co- doping with nickel and zinc. *Chem. Mater.* **27**, 408–413 (2015).
27. Heo, J. *et al.* Design meets nature: Tetrahedrite solar absorbers. *Adv. Energy Mater.* **5**, 1401506 (2015).
28. Sarker, J. C. & Hogarth, G. Dithiocarbamate complexes as single source precursors to nanoscale binary, ternary and quaternary metal sulfides. *Chem. Rev.* **121**, 6057 (2020).
29. Al-Shakban, M. *et al.* On the phase control of CuInS2 nanoparticles from Cu-/In-xanthates. *Dalt. Trans.* **47**, 5304–5309 (2018).
30. Zeng, N. *et al.* Rapid and low-temperature molecular precursor approach toward ternary layered metal chalcogenides and oxides: Mo 1. *Chem. Mater.* **32**, 7895–7907 (2020).
31. Murtaza, G. *et al.* Scalable and universal route for the deposition of binary, ternary, and quaternary metal sulfide materials from molecular precursors. *ACS Appl. Energy Mater.* **3**, 1952–1961 (2020).
32. Lou, W., Chen, M., Wang, X. & Liu, W. Novel single-source precursors approach to prepare highly uniform Bi 2S3 and Sb2S3 nanorods via a solvothermal treatment. *Chem. Mater.* **19**, 872–878 (2007).
33. Ajibade, P. A. & Botha, N. L. Synthesis and structural studies of copper sulfide nanocrystals. *Results Phys.* **6**, 581–589 (2016).
34. Xie, G., Qiao, Z.-P., Zeng, M.-H., Xiao-Ming, C. & Gao, S.-L. A single-source approach to Bi 2 S 3 and Sb 2 S 3 nanorods via a hydrothermal treatment 2004. *Cryst. Growth Des.* **4**, 513–516 (2004).
35. Sun, J. *et al.* Solvothermal synthesis of ternary sulfides of Sb 2-xBi xS 3 (x = 0.4, 1) with 3D flower-like architectures. *Nanoscale Res. Lett.* **5**, 364–369 (2010).
36. Xu, D., Shen, S., Zhang, Y., Gu, H. & Wang, Q. Selective synthesis of ternary copper-antimony sulfide nanocrystals. *Inorg. Chem.* **52**, 12958–12962 (2013).
37. Xu, D., Shen, S., Zhang, Y., Gu, H. & Wang, Q. Selective synthesis of ternary copper-antimony sulfide nanocrystals. *Inorg. Chem.* **52**, 12958–12962 (2013).

38. Zou, Y. & Jiang, J. Colloidal synthesis of chalcostibite copper antimony sulfide nanocrystals. *Mater. Lett.* **123**, 66–69 (2014).
39. Regulacio, M. D. *et al.* Facile solvothermal approach to pristine tetrahedrite nanostructures with unique multiply-voided morphology. *Nanoscale* **9**, 17865–17876 (2017).
40. Manimozhi, T., Archana, J., Navaneethan, M. & Ramamurthi, K. Morphology and phase controlled synthesis of PVP-assisted copper antimony sulfide microstructures using solvothermal method and their properties. *Mater. Sci. Semicond. Process.* **103**, 104606 (2019).
41. Vinayakumar, V., Shaji, S., Avellaneda, D., Aguilar-Martínez, J. A. & Krishnan, B. Copper antimony sulfide thin films for visible to near infrared photodetector applications. *RSC Adv.* **8**, 31055–31065 (2018).
42. Yang, B. *et al.* CuSbS2 as a promising earth-abundant photovoltaic absorber material: A combined theoretical and experimental study. *Chem. Mater.* **26**, 3135–3143 (2014).
43. Ramos, A. J. A., Rodriguez, V. D. L., Shaji, S., Avellaneda, D. A. & Krishnan, B. Spray pyrolysed thin films of copper antimony sulfide as photovoltaic absorber. *Phys. Status Solidi Curr. Top. Solid State Phys.* **13**, 24–29 (2016).
44. Rabhi, A., Kanzari, M. & Rezig, B. Optical and structural properties of CuSbS2 thin films grown by thermal evaporation method. *Thin Solid Films* **517**, 2477–2480 (2009).
45. Shaji, S. *et al.* Copper antimony sulfide nanoparticles by pulsed laser ablation in liquid and their thin film for photovoltaic application. *Appl. Surf. Sci.* **476**, 94–106 (2019).
46. Anastas, P. & Warner, J. *Green Chemistry: Theory and Practice.* (Oxford University Press, 2000).
47. García-Peña, N. G., Caminade, A.-M., Ouali, A., Redón, R. & Turrin, C.-O. Solventless synthesis of Ru(0) composites stabilized with polyphosphorhydrazone (PPH) dendrons and their use in catalysis. *RSC Adv.* **6**, 64557–64567 (2016).
48. Chen, Y. B., Chen, L. & Wu, L. M. Structure-controlled solventless thermolytic synthesis of uniform silver nanodisks. *Inorg. Chem.* **44**, 9817–9822 (2005).
49. Lu, L. *et al.* Effect of solid inorganic salts on the formation of cubic-like aggregates of ZnSnO 3 nanoparticles in solventless, organic-free reactions and their gas sensing behaviors. *Mater. Sci. Eng. B* **177**, 942–948 (2012).
50. Lewis, E., Haigh, S. & O'Brien, P. The synthesis of metallic and semiconducting nanoparticles from reactive melts of precursors. *J. Mater. Chem. A* **2**, 570–580 (2014).
51. Roffey, A. *et al.* Phase control during the synthesis of nickel sulfide nanoparticles from dithiocarbamate precursors. *Nanoscale* **8**, 11067–11075 (2016).
52. Hogarth, G. & Onwudiwe, D. C. Copper dithiocarbamates: Coordination chemistry and applications in materials science, biosciences and beyond. *Inorganics* **9**, 1025 (2021).
53. Inagawa, I., Morimoto, S., Yamashita, T. & Shirotani, I. Temperature dependence of transmission loss of chalcogenide glass fibers. *Jpn. J. Appl. Phys.* **36**, 2229–2235 (1997).
54. Bayliss, P., Nowacki, W., Z. Kristallogr., Kristallgeom., Kristallphys., Kristallchem., 135, 308, (1972). No Title. **135**, (1972).
55. Kruszynska, M. *et al.* Size and shape control of colloidal copper(I) sulfide nanorods. *ACS Nano* **6**, 5889–5896 (2012).
56. Cullity, B. D. & Weymouth, J. W. Elements of X-ray diffraction. *Am. J. Phys.* **25**, 394–395 (1957).
57. Lu, X. *et al.* High performance thermoelectricity in earth-abundant compounds based on natural mineral tetrahedrites. *Adv. Energy Mater.* **3**, 342–348 (2013).
58. Wang, J., Gu, M., Bao, Y., Li, X. & Chen, L. Quick fabrication and thermoelectric properties of Cu12Sb4S13 tetrahedrite. *J. Electron. Mater.* **45**, 2274–2277 (2016).
59. Zhang, Z., Fu, Y., Zhou, C. & Lai, Y. Facile synthesis of CuSbS2 blocks, and their lithium ion storage performance. *J. Electron. Mater.* **44**, 252–257 (2015).
60. Shu, B. & Han, Q. Studies on structural, optical and electrical properties of CuSbS 2 nanoparticles. *Chalcogenide Lett* **13**, 1078 (2016).
61. Sivagami, A. D., Biswas, K. & Sarma, A. Orthorhombic CuSbS2 nanobricks: Synthesis and its photo responsive behaviour. *Mater. Sci. Semicond. Process.* **87**, 69–76 (2018).
62. Buckingham, M. A., Catherall, A. L., Hill, M. S., Johnson, A. L. & Parish, J. D. Aerosol-assisted chemical vapor deposition of CdS from xanthate single source precursors. *Cryst. Growth Des.* **17**, 907 (2017).
63. Ahmet, I. Y. *et al.* Evaluation of AA-CVD deposited phase pure polymorphs of SnS for thin films solar cells. *RSC Adv.* **9**, 14899–14909 (2019).
64. Castro, J. R. *et al.* Formation of antimony sulfide powders and thin films from single-source antimony precursors. *J. Mater. Chem.* **18**, 5399–5405 (2008).
65. Alam, F. & Lewis, D. J. Thin films of formamidinium lead iodide (FAPI) deposited using aerosol assisted chemical vapour deposition (AACVD). *Sci. Rep.* **10**, 1–7 (2020).
66. Chalapathi, U., Poornaprakash, B. & Park, S. H. Growth and properties of Cu3SbS4 thin films prepared by a two-stage process for solar cell applications. *Ceram. Int.* **43**, 5229–5235 (2017).
67. Ashraf, S. *et al.* Phase-controlled deposition of copper sulfide thin films by using single-molecular precursors. *Eur. J. Inorg. Chem.* **10**, 533–538. https://doi.org/10.1002/ejic.201301008 (2014).
68. Skinner, B. J., Luce, F. D. & Mackovicky, E. Studies of the sulfosalts of copper III; phases and phase relations in the system Cu-Sb-S. *Econ. Geol.* **67**, 924–938 (1972).
69. Fernandes, P. A. *et al.* Phase selective growth of Cu12Sb4S13 and Cu3SbS4 thin films by chalcogenization of simultaneous sputtered metal precursors. *J. Alloys Compd.* **797**, 1359–1366 (2019).

Acknowledgements

Author contributions

F.M. undertook the experiments and initially drafted the manuscript. F.A. was responsible for laboratory supervision, collection of the characterisation data and general data interpretation. M.A.B. was responsible for some data analysis and manuscript preparation. D.J.L. was responsible for conceptualisation and overall supervision.

Competing interests

The authors declare no competing interests.

Additional information

Supplementary Information The online version contains supplementary material available at https://doi.org/10.1038/s41598-022-08822-9.

Correspondence and requests for materials should be addressed to D.J.L.

Reprints and permissions information is available at www.nature.com/reprints.

Publisher's note Springer Nature remains neutral with regard to jurisdictional claims in published maps and institutional affiliations.